OPTOELECTRONICS AND ADVANCED MATERIALS – RAPID COMMUNICATIONS Vol. 19, Iss. 7-8, July-August 2025, p. 328 - 336

Research on high-sensitivity metamaterial-based terahertz microfluidic sensors for biological detection

JIANJUN LIU*, LANLAN FAN, YUPING WU, JINGHUA CHEN, PU LI*
School of Intelligent Engineering, Shaoguan University, Shaoguan Guangdong, 512005, China

Terahertz (THz) analysis of living cells is a research hotspot in spectroscopy. The key challenge is mitigating water interference to enable sensitive liquid-phase sample detection. This paper presents a high-sensitivity THz microfluidic biosensor using a metamaterial absorber, designed to reduce water absorption and enhance sensitivity. The sensor chip integrates a metamaterial absorber with microfluidic channels, exhibiting two perfect absorption peaks at 0.758 THz and 1.049 THz, with a refractive index sensitivity of up to 548.67 GHz/RIU. Experiments show the sensor maintains high Q-factor and Figure of Merit (FoM). As analytes with different refractive indices flow through the channels, both resonance peaks exhibit distinct red shifts. Material detection is achieved by analyzing the redshift difference between peaks. This metamaterial-based THz microfluidic biosensor shows promise for label-free trace substance detection and offers new directions for THz biomedical research.

(Received October 6, 2024; accepted August 4, 2025)

Keywords: THz, Sensors, Detection, Microfluidic

1. Introduction

Spectroscopy has emerged as a cornerstone in biomolecular sensing, with growing demands for rapid, label-free, and ultra-sensitive detection of biomacromolecules in liquid environments. Terahertz (THz) spectroscopy has garnered significant attention in biomedical research due to its unique ability to probe molecular vibrations and dielectric properties without invasive labeling [1]. Among THz sensing technologies, metamaterial-based biosensors stand out for their exceptional sensitivity, enabling the conversion of subtle dielectric constant changes into measurable optical signals. These label-free platforms offer distinct advantages, including (1) high sensitivity to refractive index variations, (2) trace-level substance detection, (3) rapid response kinetics, and (4) operational simplicity, making them ideal for point-of-care diagnostics [2-6].

Recent advancements in micro/nano-fabrication have significantly reduced the cost of THz metamaterial sensors, accelerating their translation from lab-scale prototypes to practical applications. Notable applications include quantitative analysis of macromolecules (e.g., proteins, nucleic acids) [2-4], real-time cell viability assessment [5], and viral particle identification [6]. However, a critical challenge persists: the strong absorption of THz waves by water severely limits direct sensing of biological samples in their native liquid state. Most existing studies rely on indirect deposition-based measurements, which often compromise sample viability and hinder accurate characterization of dynamic biological processes.

Microfluidic chip technology has emerged as a promising solution, offering low-cost, low-volume sample handling and enhanced THz wave confinement. While recent works [7-9] have demonstrated microfluidic-enabled sensing of high-absorption solutions in the THz range, these systems still suffer from limited sensitivity due to suboptimal electromagnetic field localization. This study addresses this gap by integrating a metamaterial absorber with a microfluidic channel, leveraging Fabry-Pérot resonance to enhance field confinement and achieve high-sensitivity detection of liquid-phase analytes.

Microfluidic technology has revolutionized sensing by enabling detection at the micro/nanometer scale, with demonstrated applications in biomolecular analysis [10-11]. The integration of metamaterial absorbers with microfluidic channels introduces a paradigm for terahertz (THz) sensor design, leveraging the Fabry-Pérot (F-P) resonance mechanism to enhance electromagnetic field confinement. Upon THz wave incidence, the metamaterial’s F-P structure traps incident energy within the absorber cavity, where the microfluidic channel—serving as both the dielectric layer and analyte reservoir—aligns with the high-field region. This spatial overlap significantly amplifies local electromagnetic fields, thereby enhancing the sensitivity to analyte refractive index changes. Additionally, the microfluidic channel’s sub-microliter volume minimizes water-induced THz absorption, enabling high-fidelity detection of liquid-phase samples [12].

This study demonstrates a dual-resonant THz microfluidic biosensor based on metamaterial absorption, achieving two near-ideal absorption peaks (absorptivity

≥99.9%) at 0.758 THz and 1.049 THz within the 0.5–1.2 THz range. The sensor's ability to resolve refractive index variations with high sensitivity (up to 548.67 GHz/RIU) and maintain robust performance metrics (Q-factor, FoM) highlights its potential for label-free trace substance detection in biomedical applications, including glucose monitoring, cancer biomarker analysis, and dynamic cellular studies [13-14]. By merging metamaterial engineering with microfluidic precision, this work establishes a versatile platform for advancing THz-based point-of-care diagnostics.

2. Structural design

Fig. 1(a) shows the unit structure of the metamaterial-based terahertz microfluidic biosensor absorber. The sensor consists of five layers, arranged from top to bottom as follows: dielectric layer, metal microstructure, microfluidic channel, metal reflective layer, and substrate. The dielectric layer is made of quartz material with a dielectric constant of $\varepsilon=3.75+i0.015$ and a thickness of 4 μm. Both the metal layer and the metal reflective layer are made of gold with a conductivity of $\delta=4.52\times10^{7}$ S/m and a thickness of 0.1 μm. The substrate is made of silicon, which does not affect the sensor's performance, with a dielectric constant of 11.9 and a thickness of 50 μm. The unit structure has a periodicity of l1=120 μm. The microfluidic channel is positioned between the metal reflective layer and the metal microstructure, with a height of $h_3=5$ μm. The optimized geometric parameters of the metal microstructure of the sensor are shown in Fig. 1 (b) and listed in Table 1.

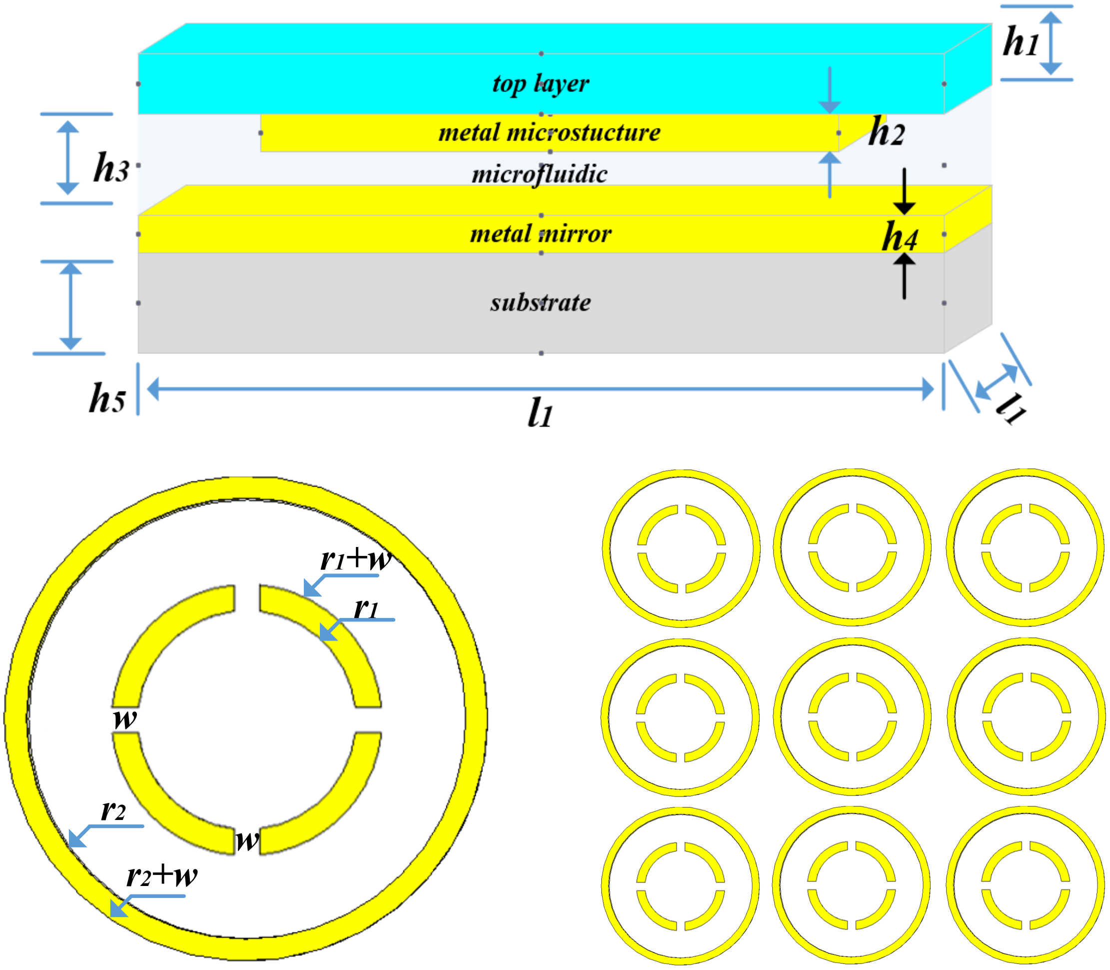

(a) Side view of the unit structure

(b) Periodic metal microstructure unit

Fig. 1. Schematic diagram of the terahertz microfluidic sensor structure (colour online)

Table 1. Geometrical parameters of the terahertz microfluidic sensor unit structure

Parameters	l_1	r_1	r_2	w	h_1	h_2	h_3	h_4	h_5
Value/μm	120	35	100	10	4	0.1	5	0.1	50

The designed structure was simulated using the electromagnetic simulation software CST Microwave Studio. When the terahertz wave is incident perpendicularly onto the surface of the structure, the electric field (E) is aligned along the y-axis, while the magnetic field (H) is aligned along the x-axis. Periodic boundary conditions were applied along both the x and y axes. The simulated S-parameters can be used to calculate the absorption rate of the absorber for the terahertz waves. According to the characteristics of electromagnetic absorption, the formula for the absorption rate is as follows: $A(\omega) = 1 - R(\omega) - T(\omega)$。. The reflectivity is given by $R(\omega) = |S_{11}|^2$, and the transmissivity is given by $T(\omega) = |S_{21}|^2$. Given that the thickness of the bottom metal film is much larger than the skin depth of the terahertz waves, transmission of the terahertz waves is effectively blocked, allowing us to neglect $T(\omega)$. Thus, the absorption rate formula simplifies to $A(\omega) = 1 - R(\omega) = 1 - |S_{11}|^2$. Perfect absorption is achieved when the reflectivity is sufficiently low. Fig. 2 analyzes the absorption performance of the absorber in relation to the material of the dielectric layer. As shown in the figure, high absorption peaks appear at $f_1 = 0.758$ THz and $f_2 = 1.049$ THz, regardless of whether the dielectric layer is lossy or not. When the dielectric layer is lossy, the absorption rate at both resonance peaks reaches as high as 99.99%. Therefore, most of the terahertz waves incident on the absorber are absorbed through the electromagnetic resonance of the metal microstructure, with only a small portion being absorbed by dielectric losses.

As shown in Fig. 3, the schematic diagrams of the magnetic field distributions on the surfaces of the channel and the cover layer correspond to the dual-ring structures that induce low-frequency and high-frequency resonances, respectively.

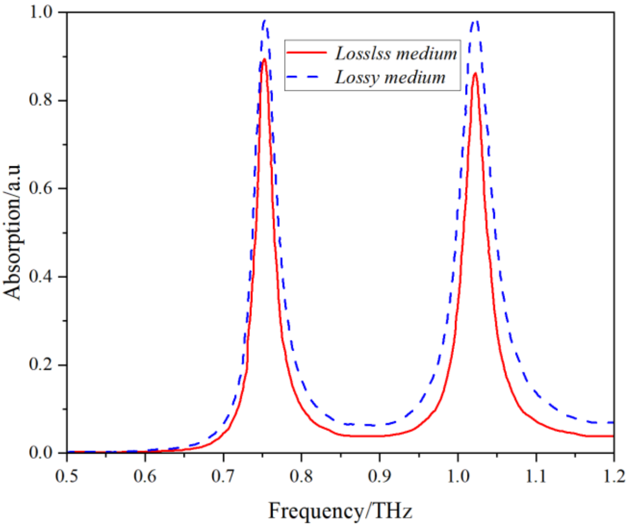

Fig. 2. Absorption curves corresponding to lossy and lossless media (colour online)

It can be seen from the figures that almost all the electromagnetic field energy of the dual-ring structures is confined within the cavity, i.e., the microfluidic channel. Since the microfluidic channel serves both as the dielectric layer of the absorber and the flow region for liquid samples, the interaction zone between the analyte and terahertz waves perfectly overlaps in space. As a result, subtle changes in the refractive index within the channel will be reflected in the shifts of the absorption peaks, demonstrating higher sensitivity.

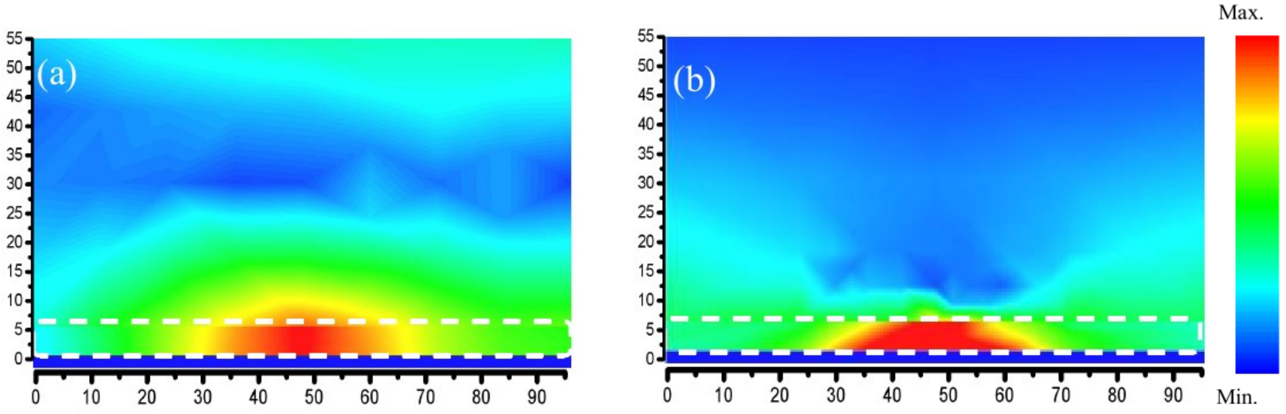

Fig. 3. The electric field and surface current distributions of the dual-ring structure at 0.758 THz (a,) and 1.049 THz (b) (colour online)

3. Results and discussion

3.1. Absorption mechanism analysis

By analyzing the electric field and surface current distribution at the resonance frequency, the physical mechanism behind the sensor's absorption peaks can be explored. When the metal microstructure consists of a single metallic ring structure (either a circular ring or a defective circular ring), the sensor's absorption spectrum is shown in Fig. 4. As can be seen from Fig. 4, the absorption peaks formed by the sensor when the micro-metal structure is a circular or defective circular ring correspond to the low-frequency and high-frequency absorption peaks observed in the combined metal structure.

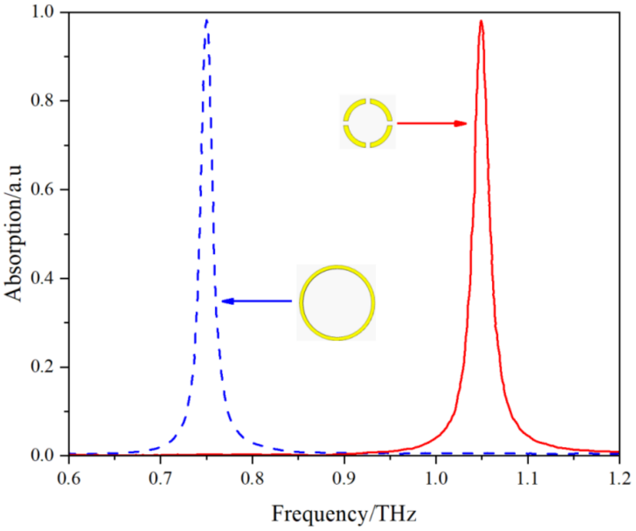

Fig. 4. Absorption spectrum of the sensor under a single-metal structure (colour online)

Fig. 5 shows the equivalent circuit of the sensor. In the equivalent circuit diagram, both the circular and defective circular metal ring structures in the metal microstructure are considered as RLC series circuits. The impedance of the two can be expressed as $Z_n = R_n + j\omega L_n + 1/(j\omega C_n)$, where R_n is the equivalent resistance, L_n is the equivalent inductance, and C_n is the equivalent capacitance.

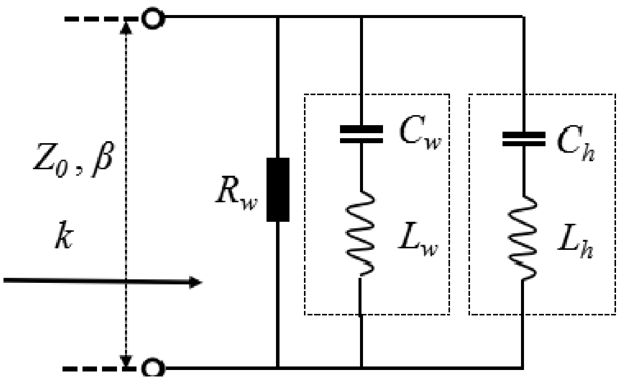

Fig. 5. Equivalent circuit of the sensor

Fig. 6 shows the complex impedance spectrum of the sensor. At the resonance frequencies of 0.758 THz and 1.049 THz, the complex impedance of the sensor is $Z_1^{'} = 0.996 - i0.0297$ and $Z_2^{'} = 1.046 + i0.253$, respectively, while the complex impedance of free space is $Z_0^{'} = 1$. Thus, the sensor achieves good impedance matching with free space, resulting in two high-absorption resonance peaks.

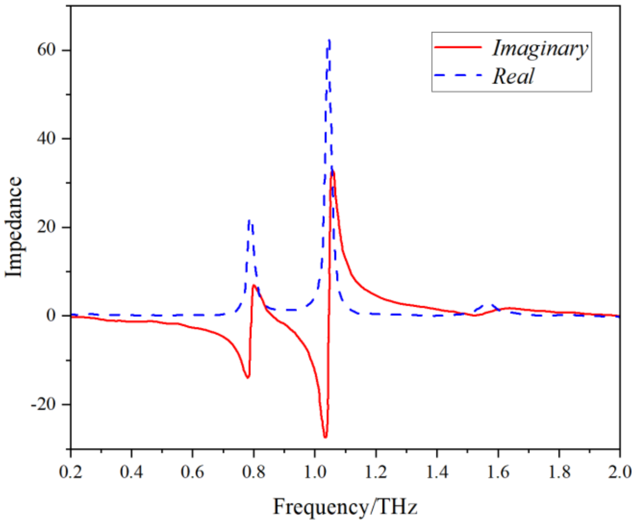

Fig. 6. The complex impedance spectrum of the sensor (colour online)

4. Results and discussion

4.1. Sensing mechanism

From the sensor's equivalent circuit, it can be seen that the sensor contains two RLC series circuits, and the absorption peaks of the sensor can be attributed to LC resonance. The resonance frequency of the LC circuit can be expressed as $f_n = 1/(2\pi L_n C_n)$, where L_n is the equivalent inductance and C_n is the equivalent capacitance. Once the parameters of the sensor's structural unit are fixed, C_d remain constant. When the dielectric constant of the analyte in the microfluidic channel changes, it causes a variation in the capacitance, which in turn alters the equivalent capacitance. This ultimately results in a shift in the resonance frequency *f*, allowing detection of the analyte by measuring the degree of frequency shift.

Sensitivity is an important metric for evaluating sensor performance, and it is calculated using the formula $S=\Delta f/\Delta n$, with units of GHz/RIU. Here, Δf represents the frequency shift, and Δn denotes the change in the refractive index of the analyte. In addition to sensitivity, the Q-factor and Figure of Merit (FoM) are also key indicators of sensor performance. The Q-factor represents the resonance strength between the terahertz wave and the sensor, with a higher Q-factor indicating stronger resonance. It is calculated using the formula Q = f_0 /FWHM, where f_0 is the resonance frequency and FWHM is the full width at half maximum of the resonance peak. The FoM characterizes the overall performance of the sensor, with a larger FoM value indicating better overall performance. The FoM is expressed as FoM = S/FWHM, with units of RIU^{-1}, where S represents the sensor's sensitivity.

4.2. Sensor performance

The sensor's multilayer structure effectively confines the energy of the incident terahertz waves into the microfluidic channel, forming an F-P resonance cavity and locally enhancing the electromagnetic field within the channel. The analytes in the microfluidic channel enhance their interaction with the local electromagnetic field. This multilayer sensor structure offers superior sensing performance compared to transmission-based sensors using metasurfaces. Fig. 8 shows the effect of analytes with different refractive indices on the sensor's performance. In Fig. 7 (a), the absorption spectra of the sensor under different refractive indices are presented. As seen in Fig. 7 (a), with an increase in the refractive index of the analyte, the resonance frequency decreases, causing a significant redshift in the sensor's absorption peaks. The frequency shift of the low-frequency and high-frequency absorption peaks is shown in Fig. 7 (b). As the analyte's refractive index increases, the frequency shift of the sensor's absorption peaks also increases. The effect of the analyte's refractive index on the sensor's Q-factor and FoM is shown in Figs. 7 (c) and 7 (d). From Figs. 7 (c) and 7 (d), it can be observed that as the refractive index increases, the Q-factor and FoM of the high-frequency absorption peak increase slightly, while the Q-factor and FoM of the low-frequency absorption peak exhibit minor fluctuations. The maximum Q-factor of the sensor is 38.6, and the maximum FoM is 24.5RIU^{-1}.

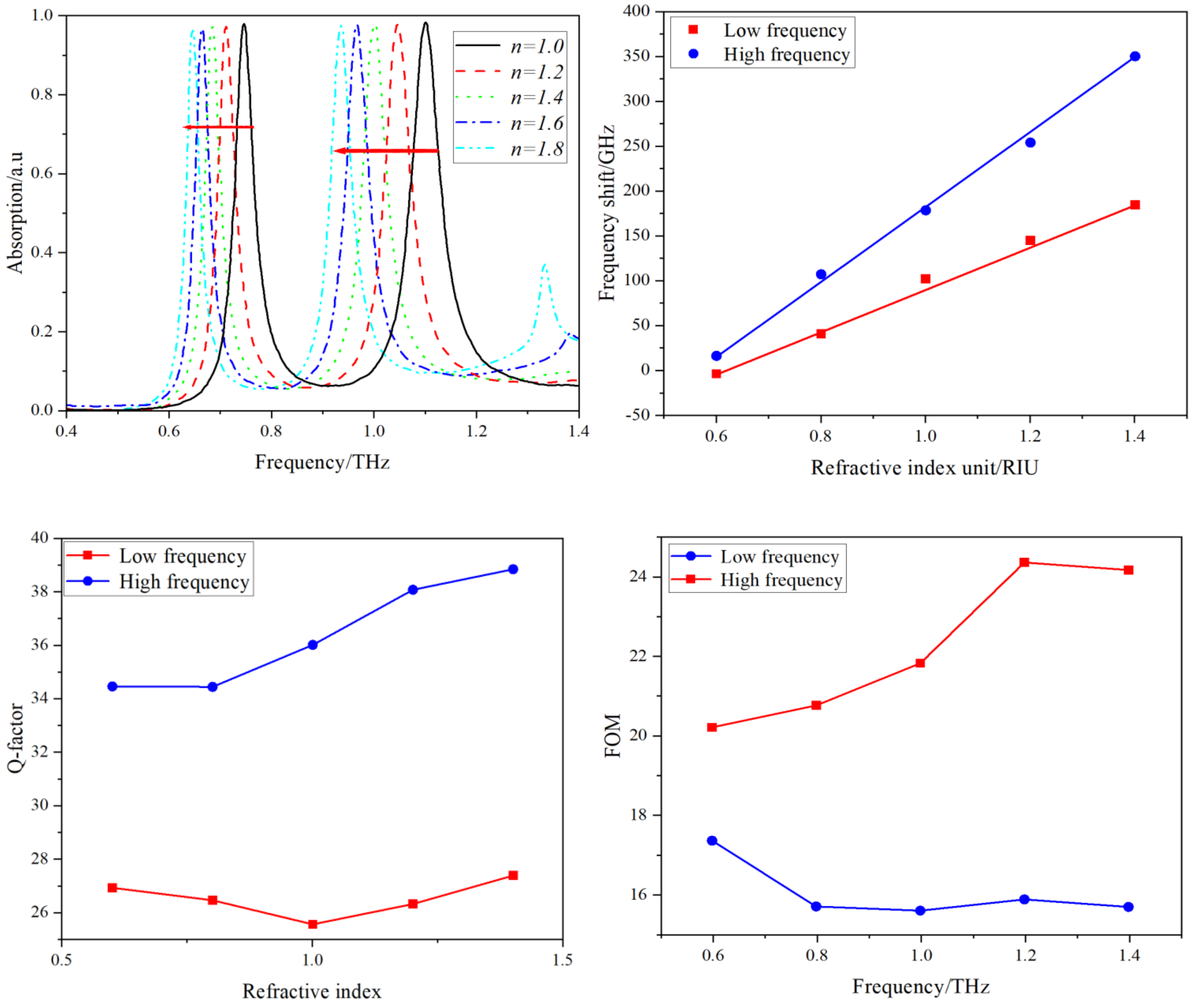

Fig. 7. The effect of analytes with different refractive indices on the sensor's sensing performance (colour online)

The sensor, integrated with a microfluidic channel, enables the detection of analytes in solution, simplifying the detection process and reducing the detection time, thus achieving rapid substance detection. When the real part of the dielectric constant of the analyte is 1, the effect of the analyte's loss tangent on the sensor's absorption spectrum is shown in Fig. 8. As can be seen from the figure, as the loss tangent of the analyte increases, the sensor's resonance frequency remains unchanged, but the absorption rate decreases significantly. The increase in the loss tangent of the analyte weakens the resonance strength of the sensor, reducing its ability to absorb the incident wave. Consequently, the FWHM and Q-factor of the absorption peak decrease as the loss tangent increases. Therefore, the sensor can distinguish the changes in the loss tangent of the analyte by monitoring the changes in the absorption rate and Q-factor. Overall, the sensor maintains a relatively high Q-factor and FoM under different refractive index analytes.

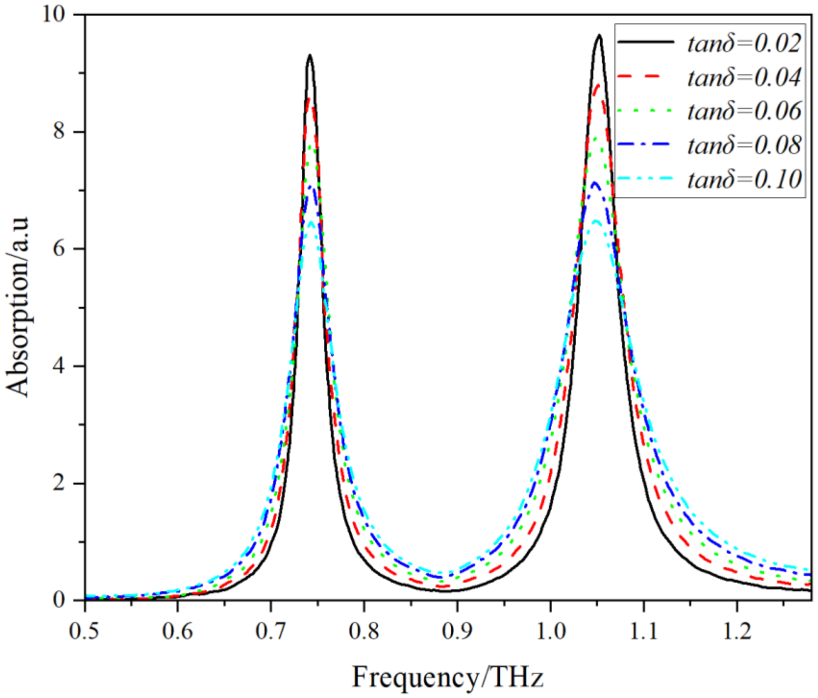

Fig. 8. The effect of the analyte's loss tangent on the sensor's absorption spectrum (colour online)

Table 2 shows a comparison of the sensitivity of the proposed sensor with terahertz sensors designed in the referenced literature. The results indicate that, within a similar terahertz frequency range, the sensitivity of the sensor proposed in this paper is significantly higher, demonstrating excellent potential for application in the field of terahertz sensing.

Table 2. Comparison of the sensor proposed in this paper with sensors from the referenced literature

References	Resonance frequency/THz	Sensitivity	Q-factor	FOM	Absorptivity
[15]	2.249	300GHz/RIU	22.05	2.94	99%
	13	4.2THz/RIU	/	12.5	/
[16]	0.76	470GHz/RIU	14.4	3.7	/
	1.28	510GHz/RIU	23	9.4	/
[17]	0.79	379GHz/RIU	53	25	/
[18]	/	192GHz/RIU	/	/	98.8%
[19]	/	312GHz/RIU	25.3	18.7	/
Proposed	0.758	548 GHz/RIU	15.7	6.4	99.9%
	1.049	313/GHz/RIU	25	11.2	99.9%

4.3. The effect of microfluidic channels and dielectric layers on sensor performance

The multilayer structure design of the sensor causes a portion of the incident terahertz waves to undergo multiple reflections between the metal microstructure layer and the metal reflective layer. These terahertz waves are confined within the microfluidic channel, forming an F-P resonance, thereby enabling absorption of the terahertz waves. The strength of the resonance absorption depends on the degree of impedance matching between the sensor's equivalent impedance and the free space impedance. By adjusting the height of the microfluidic channel, the sensor's equivalent impedance can be altered to achieve good matching with the free space impedance, thereby enhancing the absorption of terahertz waves. To this end, with other parameters unchanged, the effects of different microfluidic channel heights ($h3 = 2\sim10\ \mu m$) on the sensor's absorption peak FoM value, Q-factor, and absorption rate were studied. The simulation results are shown in Fig. 9.

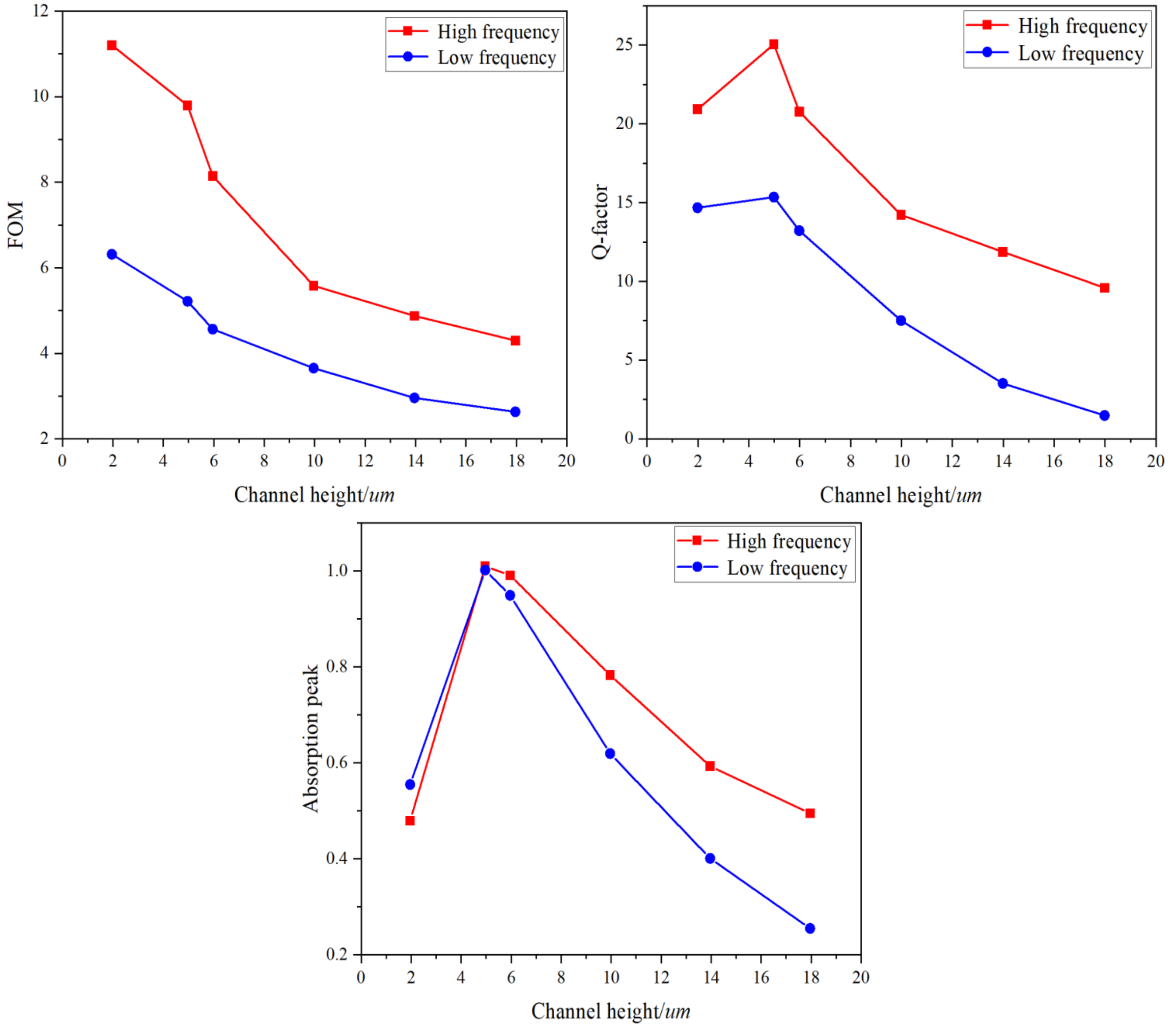

Fig. 9. Relationship between the FoM value, Q-factor, and absorption peak values of the low-frequency and high-frequency absorption peaks as a function of channel height (colour online)

As shown in the figure, both the Q-factor and FoM values for low and high frequencies decrease with increasing channel height. Additionally, the Q-factor and FoM values for high frequencies are significantly greater than those for low frequencies, with the high-frequency Q-factor and FoM values being 25 and 11.2, respectively, while the low-frequency Q-factor and FoM values are 15.7 and 6.4 at a channel height of 5 μm. Notably, the absorption peak reaches its maximum value when the microfluidic channel height is 5 μm, indicating that at this point, perfect absorption occurs, and the overlap between the analyte and the field is maximized.

Fig. 9 illustrates the relationship between the dielectric constant and thickness of the dielectric layer and the sensor's sensitivity. When the height of the microfluidic channel is fixed at 5 μm, Fig. 10 (a) shows that as the dielectric constant of the dielectric layer increases from 2 to 18, the sensitivity of the low-frequency resonance peak decreases from 313.18 GHz/RIU to 85.15 GHz/RIU, and the sensitivity of the high-frequency absorption peak decreases from 548.67 GHz/RIU to 211.76 GHz/RIU. Furthermore, when the dielectric constant is 2, Fig. 10(b) indicates that as the thickness of the dielectric layer increases from 4 μm to 17 μm, the sensor's sensitivity gradually decreases. Increases in the dielectric constant and thickness of the dielectric layer cause an increase in ε_d and φ, which leads to an increase in the equivalent capacitance C_d, while the ratio of capacitance $\kappa = C_a/C_n$ decreases. This reduces the frequency shift of the absorption peak for a given refractive index analyte, thereby lowering the sensitivity. However, the sensor's sensitivity does not decrease indefinitely with increasing dielectric layer thickness. When the thickness of the dielectric layer increases from 17 μm to 90 μm, the sensor's sensitivity remains constant, with the low- and high-frequency absorption peak sensitivities stabilizing at 518.93 GHz/RIU and 266.04 GHz/RIU, respectively. This is because the electromagnetic field excited by the sensor is almost entirely covered by the dielectric layer, and further increases in thickness no longer affect the equivalent capacitance of the sensor, causing the sensitivity to reach saturation.

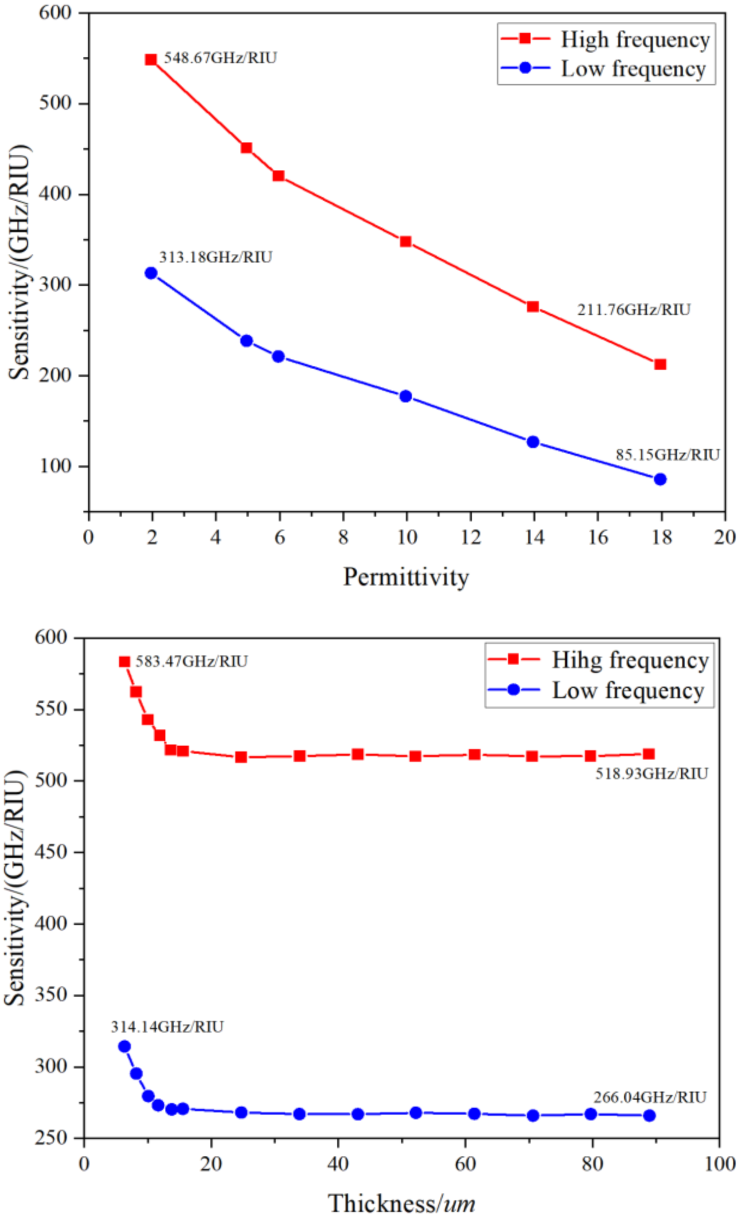

Fig. 10. Variation in the sensitivity of the sensor's low-frequency and high-frequency absorption peaks as a function of the dielectric constant and thickness of the dielectric layer (colour online)

5. Conclusion

To address the critical challenge of enhancing terahertz (THz) sensor performance for liquid-phase biomolecular detection, this study presents a metamaterial-integrated THz microfluidic sensor leveraging a Fabry-Pérot (F-P) resonance cavity mechanism. The sensor's multi-layer architecture -comprising a metallic microstructure, microfluidic channel, and reflective layer—confines incident THz waves within the channel, creating a localized electromagnetic field hotspot that maximizes analyte-wave interaction. This design achieves a peak refractive index sensitivity of 548.67 GHz/RIU at 1.049 THz, with dual-resonant absorption peaks (0.758 THz and 1.049 THz) enabling multiplexed detection of refractive index changes.

Notably, the sensor demonstrates robust stability across diverse analytes, maintaining a high quality factor (Q-factor, up to 38.6) and figure of merit (FoM, 24.5 RIU^{-1}) even as the analyte refractive index varies from 1.33 to 1.40. Its inherent polarization insensitivity and tolerance to wide incident angles (up to 60°) further enhance practical applicability in complex biomedical environments. Parametric studies reveal that optimizing the microfluidic channel height (5 μm) and dielectric layer thickness (≤17 μm) achieves near-ideal impedance matching with free space, maximizing absorption efficiency (99.9%) and field localization.

Compared to state-of-the-art THz sensors (Table 2), this design offers superior sensitivity for dual-band operation, making it particularly suitable for label-free detection of trace biomolecules such as glucose, DNA, and cancer biomarkers (e.g. microRNA-21). In future work, experimental validation with biological samples and integration of on-chip data processing will further advance its translation to point-of-care diagnostic applications.

Acknowledgements

This work is supported by Natural Science Foundation of Guangdong Province (No. 2022A1515011409); supported by Key Areas Special Project of General Universities in Guangdong Province (No. 2023ZDZX1024); supported in part by research grants from the Youth Project of National Natural Science Foundation of China (No. 52105268); supported in part by Shaoguan University Ph.D. Initiation Project (440-9900064604); supported by Shaoguan Social Development Science and Technology Collaborative Innovation System Construction Project(No. 230330178036242).

References

[1] Masahito Oh-e, Deng-Yun Zheng, Scientific Reports **12**, 5482 (2022).
[2] Xiaoyan Liu, Min Qian, Food Chemistry **349**, 129131 (2021).
[3] Bogyu Kim, Young-Uk Jeon, Joon Hyun Kang, Scientific Reports **12**, 5363 (2022).
[4] Kazunori Serita, Hironaru Murakami, Iwao Kawayama, Masayoshi Tonouchi, Photonics **6**(1), 12 (2019).
[5] M. Zhang, Z. Yang, M. Tang, Y. Liu, X. Yang, Y. Wang, Sensors **19**(3), E534 (2019).
[6] F. Yan, L. Li, R. X. Wang, H. Zhang, Z. J. Liu, Journal of Lightwave Technology **37**(4), 1103 (2019).
[7] S. T. Huang, S. F. Hsu, K. Y. Tang, C. H. Kuo, C. Y. Lee, Micromachines **11**(1), 74 (2020).
[8] S. Anwar, Physica Scripta **98**(8), 085016 (2023).
[9] Z. X. Geng, X. Zhang, Z. Y. Fan, X. L. Wang, X. Y. Liu, X. M. Li, S. H. Yu, M. Y. Miao, Scientific Reports **7**(1), 16378 (2017).
[10] Y. J. Zhang, S. F. Wang, G. C. Zhong, H. B. Wang, Y. Q. Li, X. D. Yang, Chinese Journal of Lasers **46**(6), 0614038 (2019).
[11] L. Liang, L. Wen, C. P. Jiang, X. Y. Zhang, Y. C. Wang, J. Q. Liu, Infrared and Laser Engineering **48**(2), 0203001 (2019).
[12] D. X. Wang, Y. F. Li, X. L. Ma, Y. H. Li, J. J. Liu, Y. Wang, L. L. Zhang, X. G. Liu, Nanoscale **15**(7), 3398 (2023).
[13] X. Wang, J. L. Wang, Acta Optica Sinica **40**(19), 1904001 (2020).
[14] F. Lan, F. Luo, P. Mazumder, X. Liu, Y. Liu, Y. Li, Q. Zhu, Biomedical Optics Express **10**(8), 3789 (2019).
[15] A. S. Saadeldin, M. F. O. Hameed, E. M. A. Elkaramany, A. A. El-Shenawy, M. M. A. Salama, IEEE Sensors Journal **19**(18), 7993 (2019).
[16] R. Zhang, Q. M. Chen, K. Liu, X. Y. Liu, H. B. Sun, Z. H. Zhu, IEEE Transactions on Terahertz Science and Technology **9**(2), 209 (2019).
[17] X. Wang, J. L. Wang, Acta Optica Sinica **40**(19), 1904001 (2020).
[18] Y. J. Zhang, S. F. Wang, G. C. Zhong, H. B. Wang, Y. Q. Li, X. D. Yang, Chinese Journal of Lasers **46**(6), 0614038 (2019).
[19] Chen Tao, Li Jiawei, Wang Zhaohui, Zhang Yimo, Acta Photonica Sinica **5**(1), 0116001 (2021).

---

[*] Corresponding author: lipu_300@qq.com;
liujianjun8888@hotmail.com